Contents lists available at ScienceDirect

Displays

journal homepage: www.elsevier.com/locate/displa

Smart Dimming Sunglasses for Photophobia Using Spatial Light Modulator

Xiaodan Hu[a,*], Yan Zhang[b], Hideaki Uchiyama[a], Naoya Isoyama[c], Nobuchika Sakata[d], Kiyoshi Kiyokawa[a]

[a]Nara Institute of Science and Technology (NAIST), Ikoma, Nara 6300192, Japan
[b]Shanghai Jiao Tong University, Shanghai 200240, China
[c]Otsuma Women's University, Chiyoda, Tokyo 1028357, Japan
[d]Ryukoku University, Otsu, Shiga 5202194, Japan

ARTICLE INFO

Communicated by S. Sarkar

2000 MSC:
41A05
41A10
65D05
65D17

Keywords:
Smart sunglasses
Photophobia
Light intensity modulation

ABSTRACT

We present a smart sunglasses system engineered to assist individuals experiencing photophobia, particularly those highly sensitive to light intensity. The system integrates a high dynamic range (HDR) camera and a liquid crystal spatial light modulator (SLM) to dynamically regulate light, adapting to environmental scenes by modifying pixel transmittance through a specialized control algorithm, thereby offering adaptable light management to meet the users' visual needs. Nonetheless, a conventional occlusion mask on the SLM, intended to block incoming light, emerges blurred and insufficient due to a misaligned focal plane. To address the challenge of imprecise light filtering, we introduce an optimization algorithm that meticulously adjusts the light attenuation process, effectively diminishing excessive brightness in targeted areas without adversely impacting regions with acceptable levels of luminance.

1. Introduction

Photophobia, or light sensitivity, is a common symptom of various ophthalmic and neurologic conditions, causing discomfort, headaches, or other unpleasant feelings under intense light [1, 2, 3]. This symptom can also be triggered by other factors such as the flicker of fluorescent lights or wavelength-specific light [4, 5, 6]. This study focuses primarily on photophobia resulting from heightened light intensity, exemplified by conditions like autism spectrum disorder (ASD) [7]. Anomalies related to ASD, such as larger baseline pupil sizes or aberrant pupillary light reflexes, result in an intensified perception of visual brightness [7].

Traditional remedies like tinted lenses or sunglasses, while providing some relief [16], come with their own set of challenges. For instance, it is often medically advised against wearing dark or colored glasses indoors, as patients may become dark-adapted and consequently experience increased light sensitivity [2].

Since the 1960s, Corning and S. K. Deb have pioneered the development of photochromic [17] and electrochromic [18] materials. These materials, when integrated into sunglass lenses, offer a promising solution to the issue of dark adaptation. For instance, they can induce changes in lens color in response to ultraviolet (UV) light [8] and voltage [10, 19, 13], aiding individuals in adapting to different lighting conditions. Nonetheless, photochromic materials suffer from sluggish response times, as demonstrated by a notable decrease in transmittance dropping from 83% to 10% within 30 seconds of UV exposure and taking 25 minutes to revert post-exposure [15]. Although efforts are ongoing to improve their response speeds [20], achieving a balance between high speed and high contrast remains a significant challenge. Electrochromic materials, while requiring external electricity, are significantly more responsive and sufficiently meet daily requirements. When integrated with light or UV sensors, these materials can be used to develop auto-dimming sunglasses that adjust based on ambient light conditions [12, 13]. Yet, the intricacy of redox reactions triggered by variable voltages poses challenges for fine-tuned con-

*Corresponding author: Email address: hu.xiaodan.ht1@is.naist.jp;

http://dx.doi.org/10.1016/j.displa.xxxx.xx.xxx
Received 1 May 2013; Received in final form 10 May 2013; Accepted 13 May 2013; Available online 15 May 2013

Table 1. Comparison of tint-changing sunglasses

Tint-changing sunglasses	Lens material	Optical sensor	Dimming strategy	Dimming mode	Response time [ms]
Photochromic sunglasses [8]	photochromic	×	global	binary (on/off)	30,000
Bhagavathula *et al.* (2007) [9]	liquid crystal	pinhole camera	**selective**	binary (on/off)	**50**
Ma *et al.* (2008) [10]	electrochromic	×	global	stepwise* adjustable	2,000
Dumas *et al.* (2012) [11]	liquid crystal	solar sensor	global	**flexibly** adjustable**	**50 - 100**
Chandrasekhar *et al.* (2014) [12]	electrochromic	photosensor	global	stepwise adjustable	1,000 - 8,000
Lee *et al.* (2022) [13]	electrochromic	UV sensor	global	stepwise adjustable	10,000
Ctrl eyewear [14]	liquid crystal	light sensor	global	binary (on/off)	**3.8 - 50.5**[15]
Our system	liquid crystal	camera	**selective**	**flexibly adjustable**	**50**

* Refers to changes made in distinct, predefined levels or steps, not allowing for fine-tuning between these levels.
** Allows for continuous, seamless changes, enabling precise control without distinct breaks or steps.

trol over tint or transmittance in electrochromic materials [21].

Liquid crystals, on the other hand, offer rapid and precise control over light transmittance, especially when modulated through advanced sensor setups [11, 14, 15]. By segmenting the liquid crystal into multiple independent units, each governed by a distinct electric field, spatial light modulation can be achieved at the pixel level [22]. This capability is particularly beneficial for photophobic individuals, who are not solely discomforted by glaring sunlight during the day. Indoor fluorescent lighting or the dazzle from oncoming headlights at night can be equally troubling [16]. Clearly, devices that allow for selective dimming are more advantageous in high-contrast environments or situations characterized by abrupt shifts in luminosity. For a comprehensive comparison of our system with existing tint-changing sunglasses, see Table 1.

Building upon the capabilities of liquid crystals for precise control of transmittance, researchers have delved into the application of transmissive liquid crystal displays (LCDs), a specific type of spatial light modulators (SLMs). These have been employed in a diverse array of applications including vision augmentation [9, 23], image processing [24, 25], and optical see-through head-mounted displays (OST-HMDs)[26, 27]. Bhagavathula *et al.* devised smart glasses that incorporate a transmissive LCD integrated with a complementary metal–oxide–semiconductor (CMOS) and a pinhole panel to form a pinhole camera[9]. While these glasses are capable of locating and attenuating glare, they offer only rough localization due to the limitations of the pinhole focus, falling short in accurately discerning the size and attenuating the intensity of glare. To enhance accuracy, some researchers have employed cameras as scene detectors and algorithmically calibrated these cameras with the LCD to control pixel transmittance [24, 25, 23]. While most of these algorithms can provide non-linear dimming—adjusting transmittance based on the brightness of different scenes—none have been designed based on predefined requirements for comfortable vision. Furthermore, achieving accurate selective dimming necessitates the optical focusing of the LCD lens using multiple lenses [26]. In the absence of such an optical arrangement, the dimming becomes ineffective, especially when focusing on distant objects. This ineffectiveness occurs because the occlusion mask, generated by low-transmittance pixels on the LCD, becomes blurred and out-of-focus [27]. A conventional approach to address this challenge is to enlarge the occlusion mask [24, 27], as geometric optics dictates that an occluder must be at least as large as the aperture or pupil to fully block a point at infinity. However, this expanded mask inadvertently obscures the surrounding scene, leading to the issue of over-blocking or 'occlusion leak' (as illustrated in the top-left image in Fig. 8). While Itoh *et al.* have proposed a compensation algorithm tailored for OST-HMDs, utilizing virtual images to mitigate this problem effectively [27], no optimized solution currently exists for eyeglasses.

In this paper, we present a smart sunglasses system designed to overcome these limitations. The system features selective dimming capabilities tailored to predefined requirements for comfortable vision. It incorporates transmissive LCDs and a 12-bit high dynamic range (HDR) scene camera. The higher bit depth of this HDR camera allows for a finer gradation of light intensities, which in turn enables more precise dimming to be achieved by our control algorithm. The scene camera captures the intensity of the surrounding environment, dynamically generating an occlusion mask of low-transmittance pixels on the LCD to filter incoming light.

Our main contributions include the following:

- A compact architecture of smart sunglasses for photophobia.
- A control algorithm that meets requirements for comfortable vision and operates solely based on input from the scene camera.
- An eyeglasses-specific optimization strategy aimed at addressing the issue of insufficient dimming due to a blurred occlusion mask.

2. System Architecture and Algorithms

In this section, we outline the architecture and key methods of our smart sunglasses system. We cover the benchtop prototype designs in Section 2.1, delve into the control algorithm (Section 2.2)—including its radiometric basics and modulation functions—and conclude with our unique optimization algorithm in Section 2.3 for precise light attenuation.

2.1. Benchtop Prototype Designs

We first built a benchtop prototype (Fig. 1(bottom left)) to test and evaluate the system. The benchtop prototype is composed of two parts; a light modulation part and an illuminance detection part (Fig. 1(right)). The former consists of a primary transmissive LCD, which displays an occlusion pattern for a human eye, and the latter consists of an HDR scene camera (SC) with a 12-bit depth for capturing a finer gradation of light intensities, as discussed in Section 1, and a secondary LCD with uniform transmittance that are positioned just above the primary LCD to minimize the parallax. Both LCDs operate in conjunction with a polarizer. To simulate human vision, an eye-simulating camera (EC), which is configured with the same model as the SC, is also incorporated into this prototype setup. We placed the two cameras close together to maximize the field of view (FOV) while avoiding the introduction of a beam splitter.

The strategic placement of the SC behind an identical LCD panel with uniform transmittance is deliberate. It is designed to capture optical artifacts, including diffraction and variations in transmittance. By incorporating these artifacts into the modulation algorithm, the occlusion pattern is adjusted to compensate for them as much as possible, thereby ensuring that the captured scene more closely aligns with the user's perception.

Subsequently, we designed a wearable prototype (see Fig. 1, top left). In this configuration, LCDs serve directly as lenses, and the SC is positioned behind one of them to share a similar structure of the benchtop prototype. Placing the camera at the corner of the LCD, rather than at the center, was a decision aimed at maintaining the compactness and wearability of the sunglasses. This design choice avoids the need for an additional LCD—which would act as the secondary LCD in the benchtop prototype and add to the system's bulkiness—thereby allowing the SC in the corner of the LCD to provide an unobstructed view for the user and contribute to a lighter form factor. Additionally, we can choose not to display the occlusion pattern in the corner of the LCD that is directly in front of the SC, upholding the uniform transmittance approach utilized in the benchtop prototype.

The workflow is illustrated in Fig. 1 (right). The SC captures the real environment through the secondary LCD. An occlusion mask is then computed and displayed on the primary LCD, allowing the EC to capture images with balanced contrast.

2.2. Control Algorithm

2.2.1. Radiometric Basics

Both human eyes and cameras function by allowing light to pass through a set of lenses, finally reaching a light-sensitive area. In humans, it's the retina; in cameras, it's the image sensor. The sensor converts the incoming light into an electrical signal that is then digitized.

As shown in Fig. 2(b), light attenuates when passing through an SLM. The original radiance L becomes L', subject to the transmittance T of the SLM:

$$L' = TL.$$

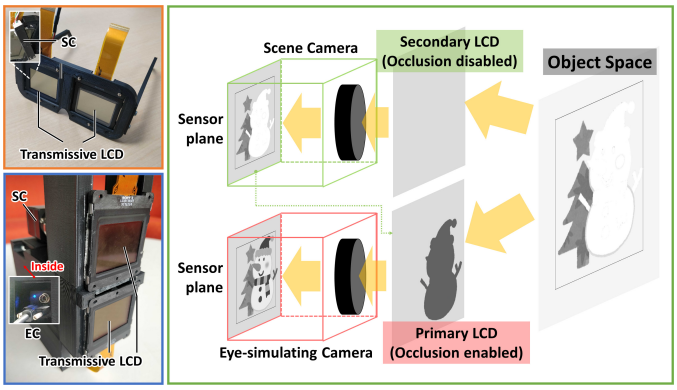

Fig. 1. (Top left) A proposed smart dimming sunglasses design with an integrated mini scene camera (SC) behind the lens for real-time environmental sensing. (Bottom left) A benchtop prototype setup is used for system evaluation, focusing on light capture and modulation. (Right) The workflow illustrates how the SC first senses the environment through a secondary LCD with uniform transmittance. This data informs the computation of a dynamic occlusion mask, which is then displayed on the primary LCD. Consequently, the eye-simulating camera (EC) perceives the scene with an optimized contrast level on its sensor plane.

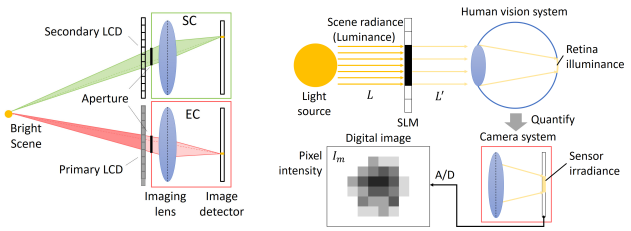

(a) Optical layout (b) Schematic figure

Fig. 2. Optical layout and schematic representation of the proposed system. (a) Two homographic mappings are depicted: one from the primary LCD (for selective dimming) to the image detector of the eye-simulating camera (EC), and the other from the image detector of the scene camera (SC) to the EC. (b) The sensed scene radiance, L, undergoes attenuation by the SLM to L', directing the modified light towards the user's eye. For system calibration and evaluation, the camera's sensor captures the attenuated radiance L', translating it into sensor irradiance and ultimately into a digital signal characterized by pixel intensity I_m.

For our camera-based system, exposure time linearly affects the amount of radiance reaching the image sensor. We assume that the attenuated radiance L' is linearly related to sensor irradiance. Therefore, the pixel intensities captured by the EC and the SC can be represented as:

$$I_{EC} = f_r(L') = f_r(TL), I_{SC} = f_r(T_{max}L), \quad (1)$$

where I_{EC} and I_{SC} denote the pixel intensities captured by the EC and the SC, respectively. The secondary LCD provides uniform dimming, and its transmittance can be approximated as a constant value T_{max}. The response function f_r can be determined through measurements with a luminance meter.

The transmittance T is related to the voltage applied to the liquid crystal elements in the LCD. However, as accessing the voltage for each element is impractical, we use pixel intensity I_m on the LCD as a proxy. We quantity the transmittance T with a certain grayscale value I_m on the LCD by placing a luminance meter after the LCD to measure the attenuated lumi-

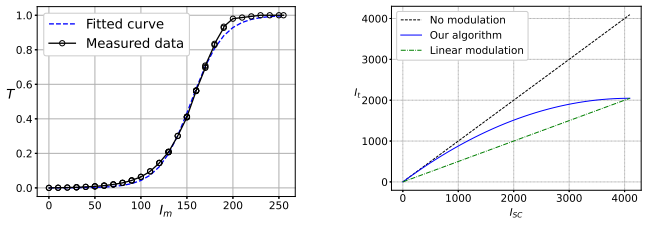

(a) Attenuation efficiency (b) Modulation function

Fig. 3. (a) The relationship between the transmittance (T) of the LCD we use and the pixel intensity (I_m) of the occlusion mask can be fitted by a sigmoid function. (b) Modulation functions between original (I_{SC}) and target (I_t) pixel intensities; no modulation (dashed), linear moduldash-dot), and parabolic modulation (solid).

nance, which is shown in Fig. 3(a) (This measurement result depends on the devices, we give the detailed configuration in Section 3.1). The relationship can be fitted by a sigmoid function f_s as:

$$T = f_s(I_m). \tag{2}$$

2.2.2. Modulation Function

In our system, the sole input is the image intensity I_{SC}, derived from the sensor irradiance captured by the SC. The target image intensity on the EC, denoting the perceived brightness for a human observer, is designated as I_t. As per Eq. (1), I_t can be formalized as:

$$I_t = f_r(T_t L), \tag{3}$$

where T_t is the target LCD transmittance for obtaining I_t.

We define the attenuation ratio a_t as the quotient of I_t over I_{SC}:

$$a_t = \frac{I_t}{I_{SC}}, \tag{4}$$

This ratio represents the relative change in image intensity before (I_{SC}) and after modulation (I_t).

Fig. 3(b) delineates the modulation functions. The dashed and dash-dot lines signify the mappings for unmodulated and linearly modulated cases, respectively. Both are uniform modulations that reduce each pixel intensity by a consistent attenuation ratio.

For alleviating the symptoms in photophobic individuals without introducing visual disturbances, we propose the following criteria for computing the occlusion mask:

- High-intensity regions should be comfortably dimmed yet discernible,
- Low-intensity regions should be minimally altered,
- Regions with higher (lower) intensity should appear brighter (darker) after modulation.

These criteria are embedded in our modulation function, which is designed to:

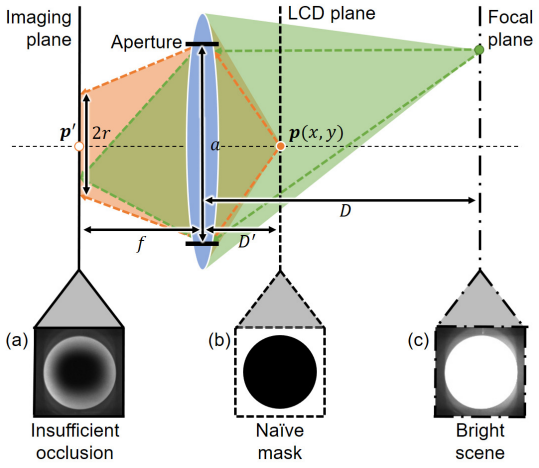

Fig. 4. The imaging process of the proposed system. While the LCD panel is not in the focal plane, a pixel p on the LCD plane can be imaged as a blurred disc with p' as the center and r as the radius. With the real bright scene (c), the computed naïve occlusion mask (b) is observed as an insufficient occlusion (a) that allows incoming light from the edge to penetrate the occlusion mask to induce stimuli.

- Intersect with the linear-modulation function at the highest intensity,
- Be tangent to the no-modulation function at the lowest intensity,
- Increase monotonically.

In practice, we have found that a parabolic curve, as shown in Fig. 3(b), satisfies these criteria. This curve not only addresses issues of dark adaptation and glare, but also preserves the natural brightness contrast of the scene, enabling users to easily distinguish between brighter and darker areas. This ensures a more natural and comfortable visual experience with minimal perception of artificial light modulation. Moreover, it's worth noting that the curve and criteria are not fixed and can be customized to cater to different visual needs.

Hence, using Eq. (1), (3), and (4), we can determine T_t for any given I_t, and subsequently calculate the pixel intensity I_m for the occlusion mask using Eq. (2)'s inverse:

$$I_m = f_s^{-1}(T_t). \tag{5}$$

2.3. Optimization Algorithm

2.3.1. Out-of-focus Point Spread Function

In real-world scenarios, users often focus on distant scenes. In such cases, the occlusion mask on the near LCD panel appears blurred, a phenomenon described by the out-of-focus point spread function (PSF) [28]. Fig. 4 illustrates this effect.

For a point on the focal plane, the image is in focus. In contrast, pixels on the LCD that deviate from the focal plane manifest as blurred discs in the image. For instance, a pixel p will be perceived as a blurred disc centered at p' with a radius r.

If we assume the imaging system follows a linear space-invariant model, we can describe the image formation—neglecting noise and other aberrations—as:

$$I_{EC}(x,y) = I_m(x,y) \otimes H_{OOF}(x,y), \tag{6}$$

Here, H_{OOF} represents the PSF of the imaging system, $\otimes$ stands for a convolution operator. Assuming a circular aperture and an LCD plane roughly perpendicular to the optical axis, the PSF H_{OOF} can be described as:

$$H_{OOF}(x,y) = \frac{1}{\pi r^2}\mathrm{circ}(\frac{\sqrt{x^2+y^2}}{r}). \tag{7}$$

The radius r of the blurred disc is determined by:

$$r = \frac{a}{2}\left|1 - \frac{D'}{D}\right|, \tag{8}$$

where a is the aperture diameter, and D and D' are the focal plane and LCD plane depths, respectively. In general, $D' \ll D$, simplifying Eq. (8) to $r \approx a/2$.

As shown in Fig.4, the circular occlusion mask (Fig.4(b)) is computed from the bright scene (Fig.4(c)) detected by the SC. Following a PSF, EC observes a blurred occlusion mask (Fig.4(a)) that is blurred at the edge and leads to insufficient occlusion.

2.3.2. *Optimization for the Occlusion Mask*

As previously mentioned, one conventional approach to enhance occlusion is to expand the occlusion mask by the aperture radius [24]. While effective in blocking light, this method suffers from the issue of occlusion leak, as already discussed. Itoh *et al.* offered a compensatory algorithm to mitigate this problem [27], but their solution is not viable for our sunglasses that is without a compensation by the virtual image.

In summary, utilizing the original mask leads to inadequate occlusion, while expanding it by the aperture radius results in occlusion leak, primarily because the expansion aims for complete occlusion. Therefore, it becomes crucial to identify an optimal expansion radius that allows the mask to effectively filter light without causing occlusion leak.

To tackle this challenge, we formulate a mathematical model aimed at optimizing the occlusion process. Our primary objective is to enable the central pixel to maintain its intensity without excessive degradation, thereby achieving an *effective occlusion*. Simultaneously, the model aims to ensure that these pixels do not leak beyond the intended occlusive area, leveraging the natural defocusing at the mask's edge to minimize perceptibility.

In Eq. (3), (4), and (5), we collectively describe how the scene brightness, I_{SC}, impacts the pixel intensity, I_m, displayed on the LCD panel. To illustrate this, let's consider an extreme scenario where the scene resembles an approximately binarized image, as depicted in Fig. 4(c). In this case, only the central bright region exists, surrounded by a dark area. The corresponding occlusion mask to be displayed on the LCD would also be binarized, as shown in Fig. 4(b).

We define the bright ($\mathbb{B}$) and dark ($\mathbb{D}$) regions in the image captured by the SC as follows, schematically represented in Fig. 5(a):

$$\mathbb{B} = \{(x,y) | I_{SC}(x,y) \geq t_b\}, \mathbb{D} = \overline{\mathbb{B}}, \tag{9}$$

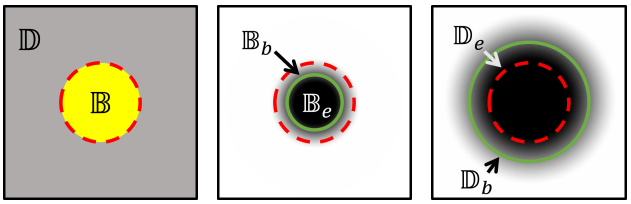

Fig. 5. Visualization of Eq. (9)-(14). (a) Schematic diagram captured by the scene camera. The bright area inside the red dashed circle represents the set $\mathbb{B}$, while the darker area outside denotes the set $\mathbb{D}$. (b) Schematic diagram from the eye-simulating camera showing insufficient mask occlusion. The green solid line differentiates the *effective* occlusion from the blurred occlusion. The area within the green solid circle is the set $\mathbb{B}_e$, and the annulus between the red dashed circle and the green solid circle represents $\mathbb{B}_b$. (c) Schematic from the eye-simulating camera where the mask is overly extensive, resulting in occlusion leak. The set $\mathbb{D}_e$ is depicted by the annulus between the green solid circle and the red dashed circle, while the blurred occlusion outside the green solid circle is the set $\mathbb{D}_b$.

where t_b is a threshold for defining the bright region and $\overline{(\cdot)}$ denotes the complement of a set.

To accomplish *effective occlusion*, we focus on the intersection of pixels that maintain their intensity within acceptable bounds with the bright region, as shown in Fig. 5(b). This set of pixels, denoted as $\mathbb{B}_e$(effective pixels with the bright region), is defined as:

$$\mathbb{B}_e = \{(x,y) \mid I_{EC}(x,y) \leq t_e(x,y)\} \cap \mathbb{B}, \tag{10}$$

here, t_e serves as a threshold determining a pixel's ability to adequately block light. It is inversely related to the derivative of the attenuation curve shown in Fig. 3(a), as given by:

$$t_e(x,y) \propto \left(\frac{\mathrm{d}f_s}{\mathrm{d}I_m(x,y)}\right)^{-1}. \tag{11}$$

Conversely, the set of blurred pixels in the bright region is expressed as:

$$\mathbb{B}_b = \{(x,y) \mid I_{EC}(x,y) > t_e(x,y)\} \cap \mathbb{B}. \tag{12}$$

Similarly, when effective and blurred pixels leak into the dark region, they can be defined as:

$$\mathbb{D}_e = \{(x,y) \mid I_{EC}(x,y) \leq t_e(x,y)\} \cap \mathbb{D}. \tag{13}$$

$$\mathbb{D}_b = \{(x,y) \mid I_{EC}(x,y) > t_e(x,y)\} \cap \mathbb{D}. \tag{14}$$

It's important to note that sets $\mathbb{B}$ and $\mathbb{D}$ are fixed, as they are determined by the static scene under study. I_{EC}, the image observed by the EC, changes if the occlusion mask is modified. We introduce the superscript α on $\mathbb{B}_e$ as $\mathbb{B}_e^\alpha$ to denote its state when the expansion radius is α.

The mask's expansion process is a morphological transformation, represented by:

$$I'_m(\alpha) = \min_{-\alpha<m,n<\alpha} I_m(x+m, y+n), \tag{15}$$

where I'_m is the expanded occlusion mask.

The optimization objective can be interpreted as maximizing the number of pixels in $\mathbb{B}_e$ while minimizing the presence of pixels in $\mathbb{D}_e$. Although pixels in $\mathbb{B}_b$ can exist, their weight for either inclusion or exclusion becomes significant as they approach or deviate from the threshold t_e. Pixels in $\mathbb{D}_b$ follow a similar rule. Combining Eq. (9) through Eq. (15), the optimization problem can be formalized as:

$$\max_{\alpha} \quad S(\alpha) = \sum_{(x,y)\in\mathbb{B}_e^{\alpha}} \sigma_1 + \sum_{(x,y)\in\mathbb{B}_b^{\alpha}} \sigma_2 \cdot (1 - 2f_s(I_{EC}(x,y)) - \sum_{(x,y)\in\mathbb{D}_e^{\alpha}} \sigma_3 - \sum_{(x,y)\in\mathbb{D}_b^{\alpha}} \sigma_4 \cdot f_s(I_{EC}(x,y)), \quad (16)$$

$$\text{s.t.} \quad \alpha \in \mathbb{Z}^+.$$

Here, σ_1 to σ_4 are the weights assigned to each pixel in the corresponding occlusion sets, and $\mathbb{Z}^+$ denotes the set of positive integers.

In terms of the weights, the contribution level of $\mathbb{B}_e$ should be highest, and thus its weight should be set to the maximum. Meanwhile, the contribution or penalty level of the other three occlusion sets can be considered roughly equal. In practice, we find that σ_1 should be set sufficiently high. Otherwise, Eq. (16) will lack an extremum. A unique extremum will manifest in Eq. (16) when σ_1 is at least three times larger than σ_2 through σ_4, as demonstrated in Fig. 7(b).

Since α represents discrete points, $S(\alpha)$ is non-differentiable. However, given that this is a discrete optimization problem, the maximum value of $S(\alpha)$ can still be efficiently found via brute-force search within a reasonable range.

3. Implementation

In this section, we describe the entire system implementation of our benchtop prototype. Our implementation covers the hardware and software setup, system calibration, and a critical algorithmic component—the out-of-focus PSF simulation. The out-of-focus simulation is integral for our optimization algorithm, allowing for controlled and precise calculations that mitigate the impacts of real-world aberrations such as noise and intensity distortions. This synergistic approach enables us to achieve high-precision, location-based selective dimming that is tailored to meet the unique needs of photophobic individuals.

3.1. Hardware and Software Setup

As depicted in Fig. 1(bottom left), our prototype employs two identical monochrome Hikvision MV-CA004-10UM cameras, equipped with SONY IMX 287 sensors (720×540 pixels, 12-bit depth), capable of a maximum frame rate of 526.5 fps. The cameras feature a 6 mm lens with an f/1.6 aperture, approximating a large baseline pupil diameter of 3.8 mm [29]. Arranged in parallel on a vertical axis, the cameras have a focal distance $D = 2$ m from both the SC and the EC. They are connected via a USB 3.0 interface and transmit video data in real-time using a multi-threaded software development kit provided by the manufacturer. To minimize reflections, the entire hardware setup is covered with a black curtain.

The primary and secondary LCDs consist of SONY LCX017 panels (36.9 × 27.6 mm active area, 705 dpi, 60 Hz, monochrome). Each of the LCD panels used in our system comprises 786,432 active dots or pixels (1024 (H) × 768 (V)), with a dot pitch of 36 µm, allowing for precise transmittance adjustment at the pixel level. Post-power-on transmittance for these panels is 21%, dropping to 10% when the linear polarizer (Edmund XP42HE-40, with a transmittance of 42.6±2%) is applied. The distance from each camera to its corresponding LCD panel is $D' = 10$ mm. The LCD panels are managed by an external driver board connected to a computer via a VGA link.

The selection of monochrome cameras is due to their higher sensitivity to light and finer granularity in detecting intensity variations. This is advantageous for our system, which relies on accurate detection of luminance changes to modulate light effectively. While the current implementation focuses on monochrome imaging, the employed SONY LCX017 LCD panels, used to serve as projector LCD panels, have inherent color processing capabilities. Moreover, these panels have been widely used in past research for see-through displays with color images [23, 27, 30], ensuring their ability to handle color images.

Our software, implemented in Python 3.8, utilizes OpenCV-Python with CUDA acceleration for system calibration and image processing. The computer configuration comprises an AMD 8-core 3.8GHz CPU and an NVIDIA GTX Titan X GPU. Leveraging GPU-based programming, our setup achieves an average rendering speed of 20 fps for generating expanded occlusion masks.

The framework of the prototype is 3D-printed in plastic, designed using Autodesk®Fusion 360 and printed by ANYCUBIC.

3.2. System Calibration

3.2.1. Calibration between the EC and the primary LCD

As shown in Fig. 2(a), the EC-to-LCD mapping adheres to a perspective model, described by a homography matrix. We adjusted the EC focus alternately between the focal and LCD planes, recording the corresponding projections. Using OpenCV-Python, we calculated the homography matrix based on these observations.

3.2.2. Calibration between the EC and the SC

Similarly, the mapping between the SC and the EC is described by a 2D homography matrix. We acquired images of an A1 size chessboard located on the focal plane using both the SC and EC, and calculated the homography matrix using OpenCV-Python functions.

3.3. Out-of-focus PSF Simulation

As shown in Fig.6, we start by displaying a static circle-shaped occlusion mask (with a 100-pixel radius) on the primary LCD. To capture a clean occlusion mask, the EC records the mask while a white background is in place before the benchtop system. Background subtraction yields the pure circle mask. Based on Eq. (6) and (7), we formulate the problem as:

$$\arg\min_{r} \|I_m \otimes H_{OOF}(r) - I_{EC}\|_2.$$

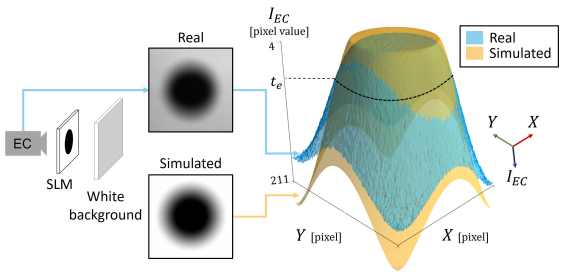

Fig. 6. (Left) The EC captures the real occlusion by positioning a white background in front of the SLM. (Middle) Result of the out-of-focus simulated occlusion mask. (Right) 3-D visualization comparing it with the real occlusion.

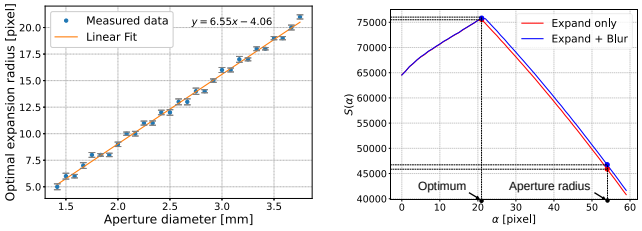

(a) (b)

Fig. 7. (a) Depicting the mapping relationship between the optimal expansion radius and the aperture diameter, enabling the system to compute an optimized mask from the user's pupil size. (b) Visualization of Eq. (16) with an optimum (extremum) at $\alpha = 21$. Our optimization model demonstrates that the function $S(\alpha)$ computed using the aperture radius is notably lower than the one derived using the optimal radius. The blue curve represents $S(\alpha)$ when an additional blurring process is incorporated. Although the optimum of $S(\alpha)$ with added blurring is greater than that of a simple expansion, the difference is not significant.

Here, the Euclidean distance is employed to quantify the similarity. To mitigate the effects of noise and diffraction aberrations originating from edge pixels, we restrict the effective calculation area to the central portion of the circle mask. It is worth noting that the simulated occlusion mask does not need to be a perfect match with the real mask, which could be distorted due to noise or diffraction. Because the primary function of the simulated mask is to serve as a performance metric, we consider the *effective occlusion* area of the simulated mask. Thus, the final simulated mask should ensure that its *effective occlusion* area closely aligns with that of the real mask, as demonstrated in Fig. 6(right). The areas of the real and simulated 3-D figures within t_e are virtually identical.

4. Experiments and Results

In this section, we demonstrate the effectiveness of our control and optimization algorithms through practical experiments conducted with our proof-of-concept system. Section 4.1 details the comparative studies of different masking techniques, including the naïve mask, aperture-based expansion mask, and our optimized mask. Section 4.2 discusses how performance varies with calibration deviations and evaluates the utility of additional blurring processes.

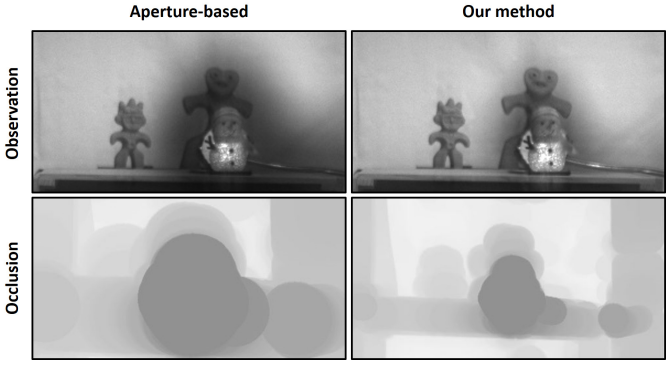

Fig. 8. Visualization of occlusion leak. By presenting a static occlusion mask on the LCD, the leak becomes pronounced when the background adopts a lighter hue.

4.1. Control and Optimization Algorithm

Our system employs a two-step approach that utilizes both control and optimization algorithms for improved performance. Initially, the control algorithm generates a naïve mask using the modulation function (shown in Fig. 3(b)) to adjust the pixel intensity, particularly aiming to suit the needs of photophobic individuals.

Following this, our optimization algorithm refines the naïve mask to mitigate occlusion leak and balance image contrast, particularly in high-contrast settings. This refinement is essential for preventing unwanted brightness and improving the visual experience, a critical need when aiming to minimize eye strain for photophobic individuals.

Utilizing the out-of-focus PSF simulated during the implementation phase, we compared the effectiveness of our method against naïve and aperture-based expansion masks. Here, the naïve mask is generated using the control algorithm but without subsequent optimization. The aperture-based expansion radius α_a is calculated as follows:

$$\alpha_a = \frac{a}{2} \cdot \frac{36.9}{1024} \approx 53.$$

In contrast, our optimization algorithm suggests an optimal expansion radius of $\alpha = 21$. The mapping between the optimal expansion radius and the aperture diameter was initially derived through simulation and was empirically validated for aperture diameters ranging from 1.5 mm to 3.75 mm, as illustrated in Fig. 7(a). Although empirical validation did not extend to aperture sizes larger than 3.75 mm due to the limitations of the 6 mm lens, the linear relationship observed within the tested range, coupled with the principles of geometric optics, suggests that system performance would likely continue in a similar linear trend for larger pupil sizes.

For the actual experiments, the camera aperture size was set to 3.75 mm and the exposure time was adjusted to 0.01s to simulate photophobic vision, resulting in a frame rate of 98.21 fps for the SC. The outcomes are detailed in Fig. 9. To assess the algorithm's ability to reduce occlusion leak, we used a translucent snowman doll illuminated by an incandescent bulb placed behind it. Additional clay statues situated behind the bulb were

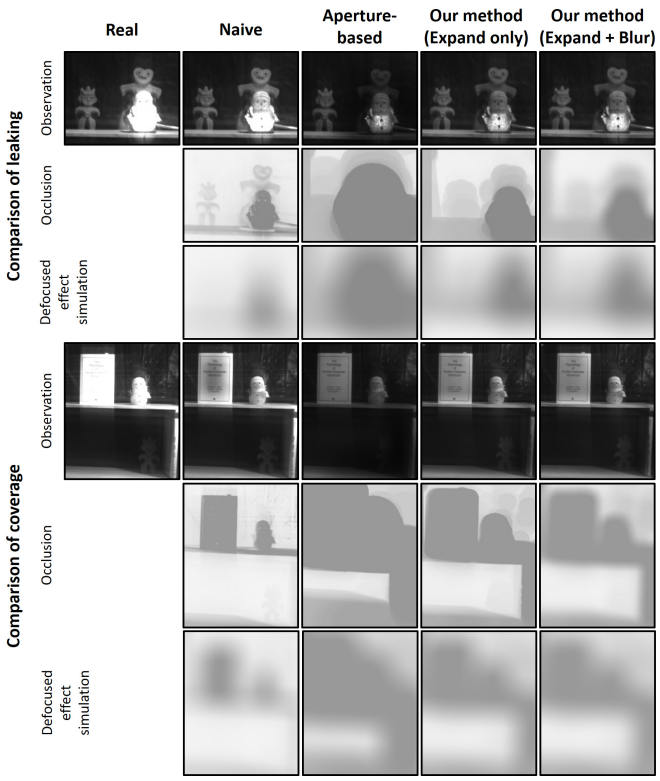

Fig. 9. Real-time observation results for the naïve mask, aperture-based expansion mask, and our proposed masks. Beneath each mask is its corresponding out-of-focus simulated effect.

lit only by ambient room light. Using the naïve mask, the snowman appeared overly bright due to the mask's limited blocking capabilities, especially when the object is out-of-focus. Conversely, the aperture-based mask, when expanded to block all incoming light, resulted in a significant occlusion leak and unintentional masking of the clay statues. The occlusion leak worsened as the backdrop color lightened, as shown in Fig. 8.

Our results conclusively demonstrate that our image-level optimization algorithm minimizes occlusion leak while maintaining satisfactory image contrast. Further tests involving a reference object with well-defined edges indicated that our algorithm excels at masking, even in conditions featuring blurry edges.

4.2. Additional Blurring Process

We further investigated the potential benefits of adding a blurring process after the mask expansion. The goal of this additional step is to soften the edges of the mask, thereby enhancing the overall masking effect. According to results obtained from our optimization algorithm, the addition of this blurring process yields higher maximum intensity values compared to simple mask expansion alone, as illustrated by the blue curve in Fig.7(b). However, the advantages of this additional process are not overwhelmingly significant, as evident from the rightmost column in Fig.9.

Subsequently, we compared the surface plots generated with and without the blurring process. Accounting for the typical calibration deviations that may occur in everyday use, we found

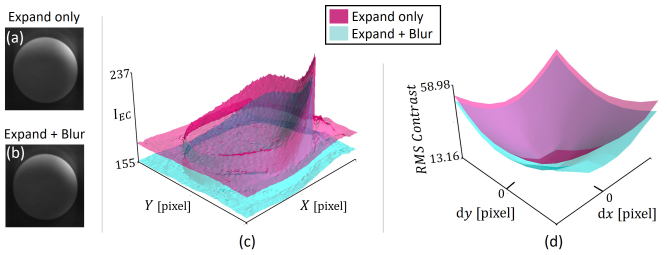

Fig. 10. (a), (b) Experiments assessing calibration deviation using two proposed masks. (c) Surface plot illustrating the corresponding occlusion effect. (d) RMS contrast comparison between the two proposed methods, evaluated across various calibration deviations. The X-axis and Y-axis represent the directions of deviation.

that a mask with blurred edges is more effective at blocking incident light at the peripheries, as depicted in Fig.10. Further calculations on the root mean square (RMS) contrast indicated that the added blurring process also somewhat reduces scene contrast, as shown in Fig.10(d).

5. Limitations and Discussion

We have demonstrated a smart dimming sunglasses system that allows real-time light modulation and balanced scene contrast to alleviate the photophobic effect. In this section, we discuss some hardware limitations, and features that have yet to be completed.

5.1. LCD panel

Diffraction. The Sony LCX017 LCD panel employed in our prototype exhibits a commendable aperture ratio of 70% and a dot pitch of 36 µm. Despite these characteristics, which suggest a diminished diffraction effect as per Yang et al. [31], diffraction remains an intrinsic challenge of LCD technology, as evidenced in Fig. 9. Our current approach to mitigating this phenomenon involves algorithmic adjustments to the occlusion pattern, based on the diffraction captured by the scene camera. While this strategy reduces the impact, it does not eliminate diffraction entirely. Innovations in pixel structure optimization have been explored as potential solutions to minimize such effects [31, 32]. Ultimately, addressing diffraction at its core may require transitioning to novel materials, such as high-response-time photochromic substances [33], which represents a significant opportunity for advancing our system in future work.

Low Transmittance. The Sony LCX017 LCD panel has a transmittance rate of 21%, presenting a challenge for our smart sunglasses application. Favored for its high resolution, individual pixel control, and cost-effectiveness, the panel has been a viable choice for our research, striking a balance between affordability and functionality. While the panel's longevity in the market attests to its practicality, enhancing transmittance is an avenue we seek to explore to improve future versions of our system. Nevertheless, for the proof-of-concept stage, the LCX017 effectively facilitates the validation of our light modulation and optimization algorithms. Looking ahead, innovations such as

the recent development of a polarizer-free liquid crystal dimmer with 70% transmittance [34], although not yet modulatable at the pixel level, offer promising prospects for elevating the performance of our sunglasses.

5.2. Wearable Design

Eye-tracking. The lightweight wearable sunglasses are easy to manufacture given the limited main components. Meanwhile, to manufacture the wearable type, eye-tracking is an essential feature. The user's pupil position is determined to shift the occlusion mask properly. To calculate and evaluate the projective transformation from the real scene to the observed scene, multiple homography matrices can be computed based on a camera system. Then, a real-time calibration between the user's eye and occlusion mask will be performed via a mapping from the camera to the user's eye.

Weight Considerations. In designing wearable devices, weight is a pivotal factor. The collective weight of the dual LCDs, camera and eye-tracker modules, along with the eyeglass frame, could approach 60g—considered on the higher end for glasses. To alleviate this, we propose relocating the compute unit and battery to an external pack, reminiscent of a portable music player or neckband headphones. This would be lightweight, transportable, and could be worn around the neck or carried in a pocket, effectively reducing the weight carried on the face to maintain comfort. The external pack, which includes the processing chip (e.g., ASIC), battery, and most driver circuitry, is estimated to weigh around 51g. Transferring these heavier elements from the glasses to the external pack is a strategic move to enhance the overall wearability of our smart sunglasses system.

6. Conclusion

We presented a smart dimming sunglasses system designed to alleviate photophobic discomfort. Our solution leverages SLM technology and a monochrome camera for real-time scene adaptation. Unlike traditional sunglasses and existing global dimming eyewear that have limitations in complex lighting scenarios, our system provides flexible, location-based light modulation. Our control and optimization algorithms allow for tailored visual experiences, enabling users to comfortably navigate varying lighting conditions without compromising visibility. Experimental results demonstrated the efficacy of our optimized masks in achieving more effective light modulation compared to naïve and aperture-based expansion techniques.

Declaration of competing interest

The authors declare that they have no known competing financial interests or personal relationships that could have appeared to influence the work reported in this paper.

Data availability

Data will be made available on request.

Declaration of Generative AI and AI-assisted technologies in the writing process

During the preparation of this work, the authors used ChatGPT in order to assist with language refinement. After using this tool, the authors reviewed and edited the content as needed and take full responsibility for the content of the publication.

Acknowledgments

This work was supported by JSPS KAKENHI Grant Number 22H00539, Japan, and JST SPRING Grant Number JPMJSP2140, Japan.

References

[1] J.E. LEBENSOHN, J. Bellows, The nature of photophobia, Archives of Ophthalmology 12 (1934) 380–390.
[2] B.J. Katz, K.B. Digre, Diagnosis, pathophysiology, and treatment of photophobia, Survey of ophthalmology 61 (2016) 466–477.
[3] R. Burstein, R. Noseda, A.B. Fulton, The neurobiology of photophobia, Journal of neuro-ophthalmology: the official journal of the North American Neuro-Ophthalmology Society 39 (2019) 94.
[4] A.J. Vincent, E.L. Spierings, H.B. Messinger, A controlled study of visual symptoms and eye strain factors in chronic headache, Headache: The Journal of Head and Face Pain 29 (1989) 523–527.
[5] P. Good, R. Taylor, M. Mortimer, The use of tinted glasses in childhood migraine, Headache: The Journal of Head and Face Pain 31 (1991) 533–536.
[6] A. Main, I. Vlachonikolis, A. Dowson, The wavelength of light causing photophobia in migraine and tension-type headache between attacks, Headache: The Journal of Head and Face Pain 40 (2000) 194–199.
[7] X. Fan, J.H. Miles, N. Takahashi, G. Yao, Abnormal transient pupillary light reflex in individuals with autism spectrum disorders, Journal of Autism and Developmental Disorders 39 (2009) 1499–1508.
[8] B. Osterby, R.D. McKelvey, L. Hill, Photochromic sunglasses: A patent-based advanced organic synthesis project and demonstration, Journal of Chemical Education 68 (1991) 424.
[9] K. Bhagavathula, A.H. Titus, C.S. Mullin, An extremely low-power cmos glare sensor, IEEE Sensors Journal 7 (2007) 1145–1151.
[10] C. Ma, M. Taya, C. Xu, Smart sunglasses based on electrochromic polymers, Polymer Engineering & Science 48 (2008) 2224–2228.
[11] J. Dumas, J. Vidal, V. Dumas, Fast response liquid crystal glasses, Lighting Research & Technology 44 (2012) 498–505.
[12] P. Chandrasekhar, B.J. Zay, C. Cai, Y. Chai, D. Lawrence, Matched-dual-polymer electrochromic lenses, using new cathodically coloring conducting polymers, with exceptional performance and incorporated into automated sunglasses, Journal of Applied Polymer Science 131 (2014).
[13] J.H. Lee, H. Kim, J.Y. Hwang, J. Chung, T.M. Jang, D.G. Seo, Y. Gao, J. Lee, H. Park, S. Lee, et al., 3d printed, customizable, and multifunctional smart electronic eyeglasses for wearable healthcare systems and human–machine interfaces, ACS applied materials & interfaces 12 (2020) 21424–21432.
[14] I. AlphaMicron, Ctrl eyewear, 2023. URL: `https://e-tintproducts.com/`, accessed: 2023-09-09.
[15] R. Zhu, H. Chen, T. Kosa, P. Coutino, G. Tan, S.T. Wu, High-ambient-contrast augmented reality with a tunable transmittance liquid crystal film and a functional reflective polarizer, Journal of the Society for Information Display 24 (2016) 229–233.
[16] J. Clark, K. Hasselfeld, K. Bigsby, J. Divine, Colored Glasses to Mitigate Photophobia Symptoms Posttraumatic Brain Injury, Journal of Athletic Training 52 (2017) 725–729.
[17] W. Armistead, S. Stookey, Photochromic silicate glasses sensitized by silver halides: Their characteristic of changing color reversibly, in combination with other properties, suggests many uses., Science 144 (1964) 150–154.
[18] S. Deb, A novel electrophotographic system, Applied Optics 8 (1969) 192–195.

[19] A.M. Österholm, D.E. Shen, J.A. Kerszulis, R.H. Bulloch, M. Kuepfert, A.L. Dyer, J.R. Reynolds, Four shades of brown: tuning of electrochromic polymer blends toward high-contrast eyewear, ACS applied materials & interfaces 7 (2015) 1413–1421.

[20] Z. Yang, J. Du, L.I. Martin, D. Van der Heggen, D. Poelman, Highly responsive photochromic ceramics for high-contrast rewritable information displays, Laser & Photonics Reviews 15 (2021) 2000525.

[21] T. Rao, Y. Zhou, J. Jiang, P. Yang, W. Liao, Low dimensional transition metal oxide towards advanced electrochromic devices, Nano Energy 100 (2022) 107479.

[22] R.R. Hainich, O. Bimber, Displays: fundamentals & applications, CRC press, 2016.

[23] Y. Hiroi, Y. Itoh, T. Hamasaki, M. Sugimoto, Adaptivisor: Assisting eye adaptation via occlusive optical see-through head-mounted displays, in: Proceedings of the 8th Augmented Human International Conference, 2017, pp. 1–9.

[24] S.K. Nayar, V. Branzoi, Adaptive dynamic range imaging: Optical control of pixel exposures over space and time, in: Proceedings of the IEEE International Conference on Computer Vision, volume 2, 2003, pp. 1168–1175. doi:10.1109/iccv.2003.1238624.

[25] G. Wetzstein, W. Heidrich, D. Luebke, Optical image processing using light modulation displays, Computer Graphics Forum 29 (2010) 1934–1944.

[26] K. Kiyokawa, M. Billinghurst, B. Campbell, E. Woods, An occlusion capable optical see-through head mount display for supporting co-located collaboration, in: Proceedings of the Second IEEE and ACM International Symposium on Mixed and Augmented Reality, 2003, 2003, pp. 133–141. doi:10.1109/ISMAR.2003.1240696.

[27] Y. Itoh, T. Hamasaki, M. Sugimoto, Occlusion Leak Compensation for Optical See-Through Displays Using a Single-Layer Transmissive Spatial Light Modulator, IEEE Transactions on Visualization and Computer Graphics 23 (2017) 2463–2473.

[28] J.W. Goodman, Introduction to Fourier optics, Roberts and Company publishers, 2005.

[29] C.J. Anderson, J. Colombo, Larger tonic pupil size in young children with autism spectrum disorder, Developmental Psychobiology 51 (2009) 207–211.

[30] Y. Zhang, X. Hu, K. Kiyokawa, N. Isoyama, H. Uchiyama, H. Hua, Realizing mutual occlusion in a wide field-of-view for optical see-through augmented reality displays based on a paired-ellipsoidal-mirror structure, Optics Express 29 (2021) 42751–42761.

[31] Q. Yang, Z. Yang, Y.F. Lan, S.T. Wu, Low-diffraction transparent micro light-emitting diode displays with optimized pixel structure, Journal of the Society for Information Display 30 (2022) 395–403.

[32] D. Manly, V. Mathur, C. Carlisle, J.A. Rolon, C. Oh, Ghost image mitigation in see-through displays with pixel arrays, U.S. Patent No. 0048676, 2021.

[33] C.W. Ooi, Y. Hiroi, Y. Itoh, A compact photochromic occlusion capable see-through display with holographic lenses, in: 2023 IEEE Conference Virtual Reality and 3D User Interfaces (VR), IEEE, 2023, pp. 237–242.

[34] J.R. Talukder, H.Y. Lin, S.T. Wu, Photo- and electrical-responsive liquid crystal smart dimmer for augmented reality displays, Optics Express 27 (2019) 18169.